Mesoporous WC_x Films with NiO-Protected Surface: Highly Active Electrocatalysts for the Alkaline Oxygen Evolution Reaction

Marvin Frisch[+],[a] Meng-Yang Ye[+],[a] Muhammad Hamid Raza,[b] Aleks Arinchtein,[a] Denis Bernsmeier,[a] Anna Gomer,[c] Thomas Bredow,[c] Nicola Pinna,[b] and Ralph Kraehnert*[a]

Metal carbides are promising materials for electrocatalytic reactions such as water electrolysis. However, for application in catalysis for the oxygen evolution reaction (OER), protection against oxidative corrosion, a high surface area with facile electrolyte access, and control over the exposed active surface sites are highly desirable. This study concerns a new method for the synthesis of porous tungsten carbide films with template-controlled porosity that are surface-modified with thin layers of nickel oxide (NiO) to obtain active and stable OER catalysts. The method relies on the synthesis of soft-templated mesoporous tungsten oxide (mp. WO_x) films, a pseudomorphic transformation into mesoporous tungsten carbide (mp. WC_x), and a subsequent shape-conformal deposition of finely dispersed NiO species by atomic layer deposition (ALD). As theoretically predicted by density functional theory (DFT) calculations, the highly conductive carbide support promotes the conversion of Ni^{2+} into Ni^{3+}, leading to remarkably improved utilization of OER-active sites in alkaline medium. The obtained Ni mass-specific activity is about 280 times that of mesoporous NiO_x (mp. NiO_x) films. The NiO-coated WC_x catalyst achieves an outstanding mass-specific activity of 1989 A g_{Ni}^{-1} in a rotating-disc electrode (RDE) setup at 25 °C using 0.1 M KOH as the electrolyte.

Introduction

Generating hydrogen through electrocatalytic water splitting is a sustainable way of obtaining clean energy.[1–3] In this reaction, the oxygen evolution half reaction (OER) shows sluggish kinetics due to its four-electron process.[4,5] The exploration of high performance OER electrocatalysts remains one of the major challenges in order to achieve highly efficient electrocatalytic water splitting.[6,7] In recent years, tremendous efforts have been paid in the pursuit of identifying highly active sites in OER electrocatalysis.[8–11] However, developing suitable catalysts and support materials for highly active sites is equally important.[12] The introduction of supporting materials enables a compensation of many limitations of the catalytically active centers, thus culminating in superior catalytic activities.[13–15] Nickel-derived oxides are known to be low-cost, highly active OER electrocatalysts in alkaline electrolyte.[16–18] Beside a high stability, the excellent OER activity of these materials has been attributed to the preoxidized Ni^{3+} on the surface of the NiO electrocatalyst.[18] The surface-exposed oxidic Ni species can be activated during OER.[9,19] However, a previous study by Bernsmeier et al.[20] indicated that a minimum electrical conductivity is often required to enable efficient electrocatalysis. Unfortunately, bulk NiO materials suffer from rather low conductivities, which hinders fast charge transportation during the reaction.[16]

In general, efficient OER catalysis requires a large number of well-accessible, highly active surface species as well as a high electrical conductivity favorable for charge transfer and a sufficient stability of the catalyst against corrosion.[21,22] A maximization of surface-exposed Ni species can be achieved by introducing a mesoporous nanostructure, for instance.[8,23,24] Moreover, the latter also provides short diffusion pathways and facilitates mass transport during catalysis.[25,26] An optimized utilization of weakly conductive NiO is targeted by employing a highly conductive carrier material.[27] Ordered mesoporous carbon or carbides could be used to provide both high electrical conductivity and high porosity, yet they suffer from oxidative corrosion during OER.[28–31] Moreover, the study of powder electrocatalysts mostly relies on the addition of binders such as Nafion.[27,32,33] The latter was shown to partially block active sites and hampers analyses of the spent catalysts.[7]

Tungsten carbides (WC_x) are highly electrically conductive,[34] earth abundant and show a promising behavior in electrocatalysis.[29,35,36] WC_x materials can be prepared by carburization of their corresponding metal oxides,[37–39] which were

[a] M. Frisch,[+] M.-Y. Ye,[+] A. Arinchtein, Dr. D. Bernsmeier, Dr. R. Kraehnert
Department of Chemistry, Technische Universität Berlin
Strasse des 17. Juni 124, 10623 Berlin (Germany)
E-mail: ralph.kraehnert@tu-berlin.de
[b] M. Hamid Raza, Prof. Dr. N. Pinna
Institut für Chemie und IRIS Adlershof, Humboldt-Universität zu Berlin
Brook-Taylor-Strasse 2, 12489 Berlin (Germany)
[c] A. Gomer, Prof. Dr. T. Bredow
Mulliken Center for Theoretical Chemistry
Universität Bonn, Beringstrasse 4, 53115 Bonn (Germany)
[+] These authors contributed equally to this work.

Supporting information for this article is available on the WWW under https://doi.org/10.1002/cssc.202101243

frequently synthesized and analyzed due to their interesting electrochromic properties.[40,41] However, typical syntheses of WC_x powders require high carburization temperatures above 800 °C, which results in pronounced crystallite growth, sintering and low surface area.[37] In contrast, soft-templated mesoporous WO_x (mp. WO_x) films enable a facile diffusion of reactive carbon species into the oxide lattice,[42,43] hence decreasing the carburization temperature and, concomitantly, preserving the mesoporosity in the obtained WC_x films (mp. WC_x).

Herein, we propose a new concept for nanostructured OER catalysts, in which the bulk consists of a Nafion-free, highly conductive, nanostructured tungsten carbide film, and the entire surface of the carbide is uniformly coated with a homogenous thin layer of NiO.

Scheme 1 outlines the overall concept. As a first step, a substrate is coated homogeneously with a nanostructured mesophase by dip-coating from a solution containing an amphiphilic triblock copolymer (PEO-*b*-PB-*b*-PEO) as a structure-directing agent[8], a metal oxide precursor (WCl_6), a complexing agent (citric acid)[44] and suitable solvents (EtOH). This mesophase is dried and then transformed into the corresponding oxide by thermal treatment in nitrogen, which leads to a concomitant removal of the template polymer and finally results in a controlled mesoporosity of the oxide film. Exposing this oxide phase to a mixture of CH_4/H_2/Ar at 700 °C induces the pseudomorphic transformation of the oxide into the respective carbide, while retaining the film integrity and its open porosity, affording a mesoporous tungsten carbide phase (mp. WC_x). ALD is used as a next step to coat the entire internal surface of the porous carbide systems with NiO (ALD-NiO/mp. WC_x).

In order to produce defined reference catalysts, templated mesoporous nickel oxide (mp. NiO_x) films were prepared by a synthesis route previously described in literature.[24] Moreover, the pore system of this mp. NiO_x as well as that of mp. WO_x were coated with a thin conformal NiO layer by a similar procedure as employed for the carbide. All catalyst films were deposited on polished titanium substrates and subsequently tested in alkaline OER (0.1 M KOH) by cyclic voltammetry in a rotating disk electrode (RDE, 1600 rpm) setup to assess activity and stability. DFT calculations were carried out to provide further evidence for the synergistic effects of the carbide carrier and the surface NiO layer. Moreover, electrical conductivity (impedance spectroscopy), crystallinity (GI-XRD, SAED), sample morphology (SEM, TEM) and local composition (EDX) as well as surface area (Kr-physisorption) were assessed.

The herein developed system has several advantages: (a) maximizing the surface exposure of Ni species, while minimizing the content of less conductive NiO, (b) providing protection of the carbide against corrosion and (c) developing a binder-free electrocatalytic system. As a result, the obtained ALD-NiO/mp. WC_x catalyst films show a low overpotential of 360 mV at a current density of 10 mA cm^{-2} in 0.1 M KOH. At a potential of 1.60 V vs. RHE, an outstanding Ni-mass based OER activity of 1989 A g^{-1}, which is ~284-fold higher than that of pristine mesoporous NiO_x films, can be achieved.

Results and Discussion

Physicochemical characterization of mp. WO_x, mp. WC_x, and ALD-NiO/mp. WC_x

We synthesized micelle-templated mesoporous WO_x films in a similar way as previously reported by Brezesinski, Smarsly and co-workers[45,46] (Figure 1a-I–c-I). The synthesis of the initial porous oxide relies on the Evaporation Induced Self Assembly (EISA) process.[47–50] The obtained mp. WO_x films were carburized in a mixture of CH_4, H_2 and Ar for 6 h at 700 °C to afford a homogeneous, macroscopically crack-free mesoporous WC_x film (mp. WC_x) (Figure 1a-II–c-II). The obtained mp. WC_x was then coated with a thin layer of NiO through ALD by alternating cycles of $Ni(Cp)_2$ and ozone (O_3) at 200 °C (Figure 1a-III–c-III). As shown in previous reports,[27,51–53] such an ALD process can ensure the deposition of a homogenous and thin particulate-

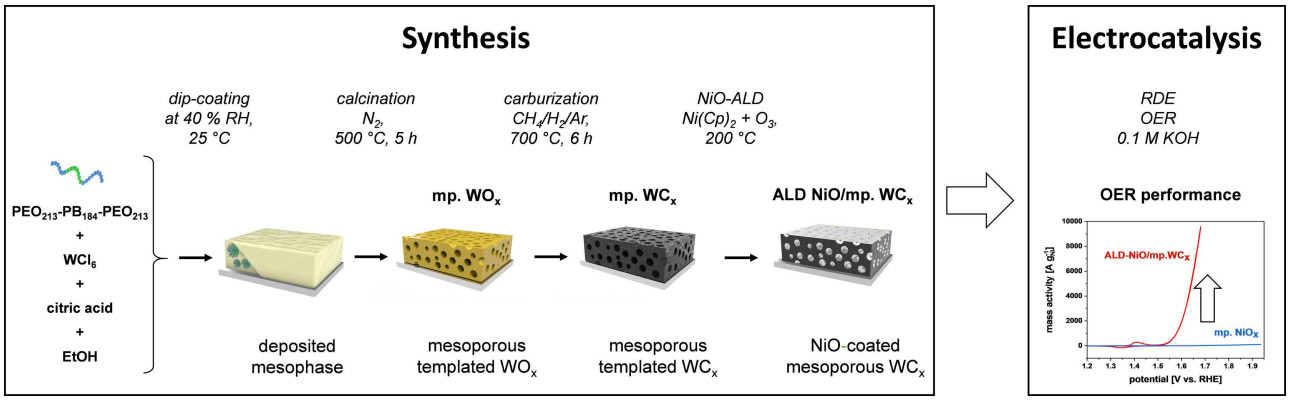

Scheme 1. Developed synthesis route for NiO-coated porous tungsten carbide catalysts. A solution containing the tungsten precursor and a micelle-forming block copolymer is deposited onto a substrate (Si, Ti, glass), dried and then calcined in nitrogen (N_2) to produce mesoporous tungsten oxide (mp. WO_x) with template-controlled porosity. This oxide phase is exposed to a mixture of CH_4/H_2/Ar at 700 °C to induce the formation of a mesoporous carbide (mp. WC_x). The carbide is then exposed in alternating cycles of $Ni(Cp)_2$ and ozone (O_3) to deposit nickel oxide (NiO) over the entire surface of the carbide's pore system to produce the final catalyst. The ALD synthesis was also applied to mp. WO_x as well as mesoporous nickel oxide (mp. NiO_x) as reference systems.

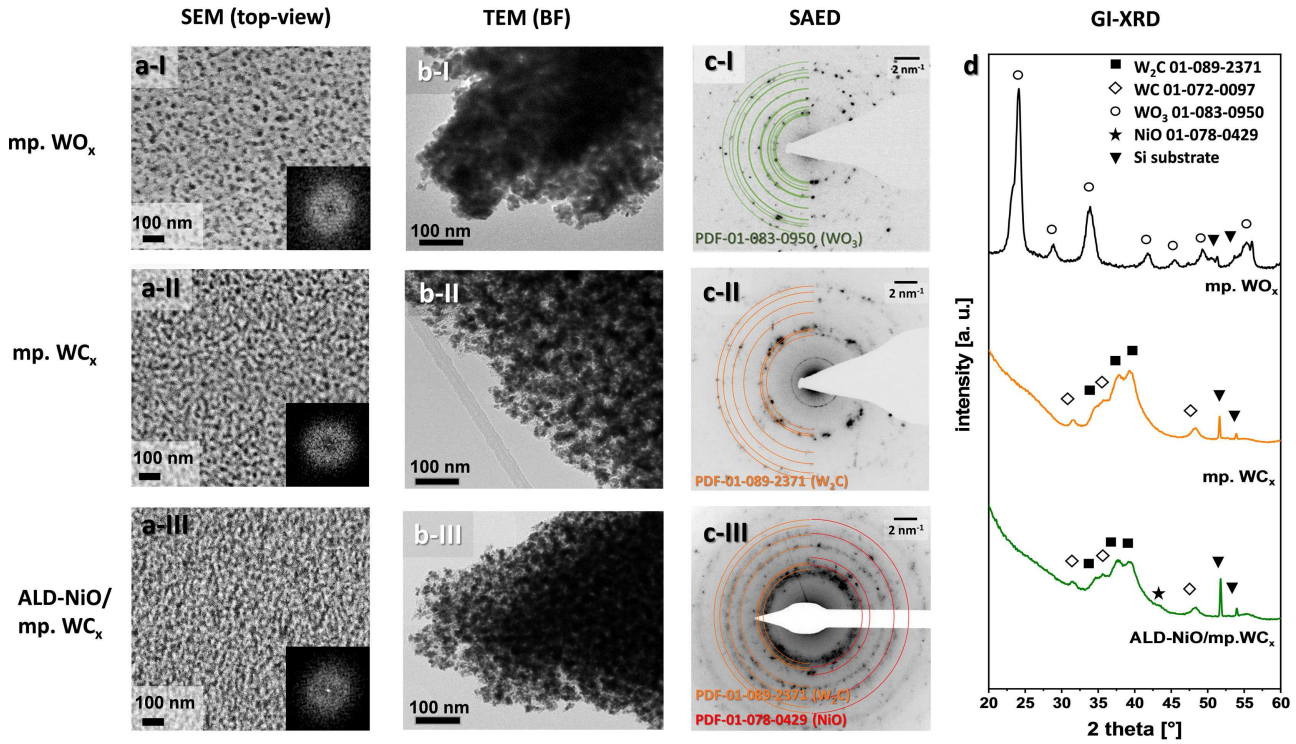

Figure 1. (a) Top-view SEM images with corresponding FFT (inset); (b) TEM images; (c) TEM-SAED patterns of mp. WO_x (I), mp. WC_x (II), and ALD-NiO/mp. WC_x (III). (d) GI-XRD patterns of mp. WO_x, mp. WC_x and NiO-ALD/mp. WC_x acquired on films deposited on Si substrates. In (d), an asterisk indicates the presence of a weak (200) lattice plane reflection of cubic NiO for NiO-ALD/mp. WC_x Electron microscopy (a, b) indicates the formation of similar mesoporous structures for mp. WO_x, mp. WC_x, and NiO-ALD/mp. WC_x. Both SAED (c) and GI-XRD (d) confirm the carburization of mp. WO_x to mp. WC_x with no remaining bulk oxide phases present, as well as the successful loading of NiO by ALD, affording NiO-ALD/mp. WC_x as a last step.

like film onto high-aspect-ratio nanostructured carriers. By changing the number of ALD cycles, the amount and thickness of the NiO coating can be precisely adjusted (for further evidence, see the Supporting Information, Section 1).[27,51,52]

Representative top-view SEM and bright-field (BF) TEM images confirm the homogenous mesoporosity of the synthesized mp. WO_x film (Figure 1a-I, b-I). The surface area of the film amounts to around 120 m^2 per geometric m^2 on average, according to BET evaluations of independent Kr-physisorption measurements.

The FFT image (Figure 1a-I, inset) shows a diffuse ring, indicating a locally ordered mesoporous structure. The SAED and GI-XRD patterns of mp. WO_x can be assigned to the WO_3 phase with minor contributions of non-stoichiometric WO_x phases (Figure 1c-I, d; PDF# 01-083-0950). Broad reflections indicate the formation of a nanocrystalline material. The XPS W4f spectrum (see the Supporting Information, Figure S2a) shows a typical doublet peak centered at 35.7 eV, indicating that the dominating tungsten species in mp. WO_x is W^{6+}, while the corresponding W–O bond centered at 530.2 eV can be observed in the corresponding O 1s spectrum (Figure S2d).[18,27]

After carburization, both top-view SEM and TEM images of the mp. WC_x film clearly portray its homogenous mesoporosity originating from the mp. WO_x precursor (Figure 1a-II, b-II). The surface area of the mp. WC_x film remains high with a value of ~100 $m^2 m^{-2}$ on average. A diffuse ring can be found in the corresponding FFT (Figure 1a-II, inset), indicating a similar structure to the mp. WO_x precursor film. The conversion from mp. WO_x into mp. WC_x can be observed from both SAED and GI-XRD patterns (Figure 1c-II, d) and the reflections can be assigned to WC (PDF# 01-072-0097) as well as W_2C (PDF# 01-089-2371). Importantly, no signs for any remaining WO_x phases are found. Broad reflections underline the preserved nanocrystallinity of the material. Beyond that, the conversion from an oxide into a carbide can be confirmed through XPS analysis of the obtained mp. WC_x after carburization (Figure S2e–h). In the W4f XPS spectrum of mp. WC_x (Figure S2e), the dominating species is indicated by a doublet peak located at 31.9 eV, which can be assigned to tungsten carbides. Only a weak signal of W^{6+} remains, which can be rationalized by a surface oxidation of the WC_x as a result of the passivation step subsequent to carburization.[54]

The deposition of NiO by ALD in the last synthesis step did not show any significant impact on the crystallinity and mesoporosity of the mp. WC_x carrier. As expected, the surface area slightly decreased to ~85 $m^2 m^{-2}$ after the deposition of NiO onto the pore walls of the carrier film, which adds evidence for the preserved mesoporosity in ALD-NiO/mp. WC_x. The GI-XRD pattern looks essentially unaltered, still showing broad reflections of W_2C and WC (Figure 1d), which can also be confirmed by SAED (Figure 1c-III). A weak reflection can be found at 43.4°, which corresponds to the (200) facet of cubic

NiO (PDF#01-078-0429). For a closer investigation of the deposited NiO layer, SAED represents a more sensitive method, clearly underlining the presence of crystalline NiO (Figure 1c-III). The typical morphology of ALD-NiO/mp. WC_x resembles that of mp. WC_x (Figure 1a-II,III, 1b-II, III). The existence of the thin NiO layer can be additionally traced by surface-sensitive XPS analysis (Figure S2i–l). Strong signals appear in the Ni 2p XPS spectrum after the ALD process, which can be addressed to typical Ni^{II} species in NiO.[27,32,55–58] In addition, the corresponding Ni–O interaction was found in the O 1s spectrum (Figure S2k).[24] Notably, Ni took up 17.65 at% of the surface element composition after ALD, while the content of W drastically reduced to 0.13 at% (Table S1), indicating that the NiO layer has covered almost the entire surface of ALD-NiO/mp. WC_x. This conclusion can be further supported by the results from bulk-sensitive WDX/StrataGem analysis, showing a significantly lower overall Ni content of 4.2 at% in the entire film volume. Note that a pronounced surface oxidation of WC_x can be observed in W4f spectrum of ALD-NiO/mp. WC_x, most likely due to the exposure to O_3 at elevated temperatures in the ALD chamber.[18] Still, the existence of WC_x species on the surface of ALD-NiO/mp. WC_x is evident. In addition, the distributions of Ni and W were investigated by using energy dispersive X-ray spectroscopy (EDX) elemental mapping coupled with TEM. A representative BF-TEM image of ALD-NiO/mp. WC_x is given in Figure 2a. The area shown in Figure 2a was analyzed by EDX spectroscopy (see the Supporting Information, Section 3). It can be observed that the signals of both Ni and W homogeneously cover the entire volume of the analyzed film fraction (Figure 2b, c), suggesting that the NiO layer is uniformly distributed over the entire surface of the mp. WC_x carrier. Furthermore, the power spectra of selected regions of a representative high-resolution HR-TEM image of ALD-NiO/mp. WC_x (Figure 2d) are typical of WC in [100] zone axis (Figure 2e) and of NiO in [100] zone axis (Figure 2f). Beyond that, lattice fringes corresponding to the {101} facet of W_2C as well as {111} and {200} facets of NiO can be observed and, importantly, the mesoporous structure of ALD-NiO/mp. WC_x is further corroborated (see the Supporting Information, Section 6).

Evaluation of OER activities, stabilities and Tafel slopes through RDE measurements in 0.1 M KOH (25 °C)

The OER activity of ALD-NiO/mp. WC_x was measured in a RDE setup through cyclic voltammetry (CV) measurements in 0.1 M KOH at RT for all samples listed in Table 1. From the electrochemical testings, Tafel slopes, Ni-based mass activities and electrochemically accessible surface areas (ECSA) of the catalysts were derived. To understand both the impact of the carrier material and the impact of the ALD process on the electrical properties, impedance spectroscopy was used to calculate the electrical sheet conductivities.

Table 1 provides an overview of the calculated electrical properties, Ni loadings and corresponding electrochemical performance data for all investigated catalyst systems. Figure 3a shows the current density-potential plots of the 30th CVs for all developed electrocatalyst systems (for further CV cycles see Figure S4). ALD-NiO/mp. WC_x exhibits by far the highest OER activity. Over 100 cycles of RDE-OER testing, ALD-NiO/mp. WC_x presents an remarkable stability, since the overpotential amounts to 360 mV at 10 mA cm^{-2} in CV 30 and well-preserved in CV 50 (368 mV, Table 1) as well as in CV 100 (372 mV, Table S2). Hence, ALD-NiO/mp. WC_x ranks amongst the state-of-the-art alkaline OER electrocatalysts in terms of overpotential in 0.1 M KOH electrolyte, yet with a significantly enhanced mass activity (Table 2). Importantly, the OER activities of the herein investigated Ni-containing electrocatalysts were normalized by

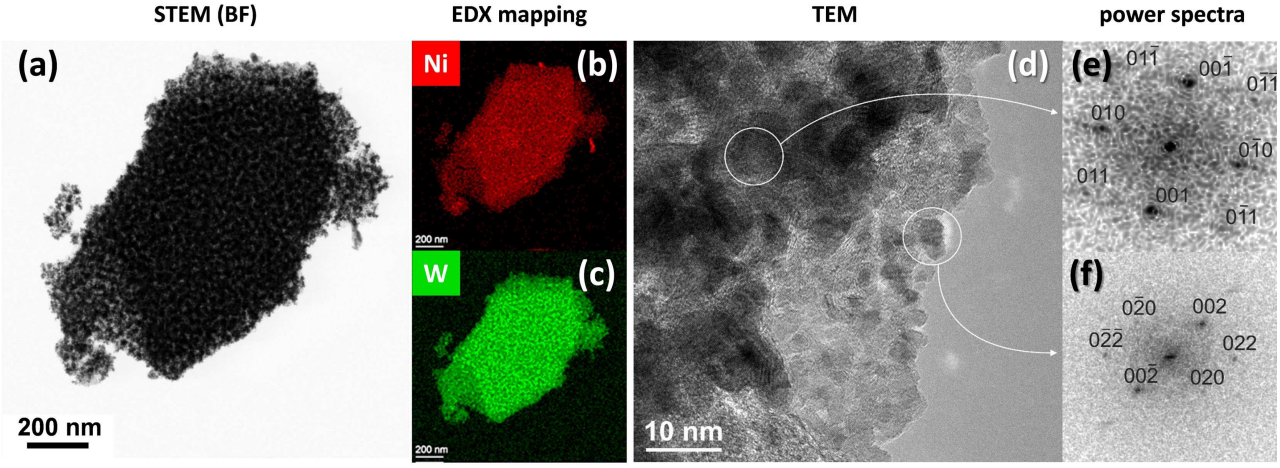

Figure 2. (a) Typical bright field (BF) STEM image of ALD-NiO/mp. WC_x. (b) Ni and (c) W EDX elemental mappings collected in the area shown in (a). (d) Representative TEM image of ALD-NiO/mp. WC_x. (e) Power spectrum of the indicated region shown in (d) typical of WC in [100] zone axis and (f) of NiO in [100] zone axis. The results from electron microscopy (a–d) suggest the formation of a nanostructured material with well-preserved mesoporosity. From the corresponding EDX elemental mappings (b, c), the homogeneous distribution of NiO species inside the pore system of the carbide carrier becomes evident. In (d), lattice fringes for both WC_x and NiO can be found. Notably, NiO is predominant at the outer surface of the material in the form of a surrounding top layer (d). For (e) and (f), two regions with crystallites showing a clear pattern were selected, as indicated by the white circles and corresponding arrows in (d).

Table 1. Electrocatalytic performance of mp. WC_x, mp. WO_x, mp. NiO_x, NiO-ALD/mp. WC_x, NiO-ALD/mp. WO_x, and NiO-ALD/mp. NiO_x.

Sample description	ALD cycle number	Ni loading[a] [µg cm^{-2} geom. area]	Sheet conductivity[b] [S cm^{-1}]	ECSA[c] [cm^2]	Overpotential [mV][d]		Mass activity (1.60 V, CV 30) [A g_{Ni}^{-1}]	Tafel slope (CV 30) [mV dec^{-1}]
					10 mA cm^{-2}, CV 30	10 mA cm^{-2}, CV 50		
mp. WC_x	0	0	$5.4\cdot10^{2}$	–	*	*	–	117
ALD-NiO/mp. WC_x	150	7 ± 1	$2.9\cdot10^{1}$	11.4	360	368	1989	57
mp. WO_x	0	0	$1.1\cdot10^{-1}$	–	–	–	–	–
ALD-NiO/mp. WO_x	150	8 ± 2	$1.1\cdot10^{-2}$	4.5	427	550	234	83
mp. NiO_x	0	33 ± 2	$3.0\cdot10^{-3}$	2.2	*	*	9	138
ALD-NiO/mp. NiO_x	150	45 ± 4	$1.4\cdot10^{-6}$	1.7	*	*	7	154

[a] Ni loading determined by ICP-OES after dissolution of the films via acid digestion. [b] Electrical conductivity investigated by impedance spectroscopy in the dark. [c] ECSA calculated from double layer capacitance C_{dl} (Figure S8). The values are stated in cm^2 per geometric cm^2 film area on extensively polished Ti substrates. [d] Asterisks denote catalysts for which the current density did not reach $j = 10$ mA cm^{-2} within the investigated OER potential window (1.20–1.95 V vs. RHE).

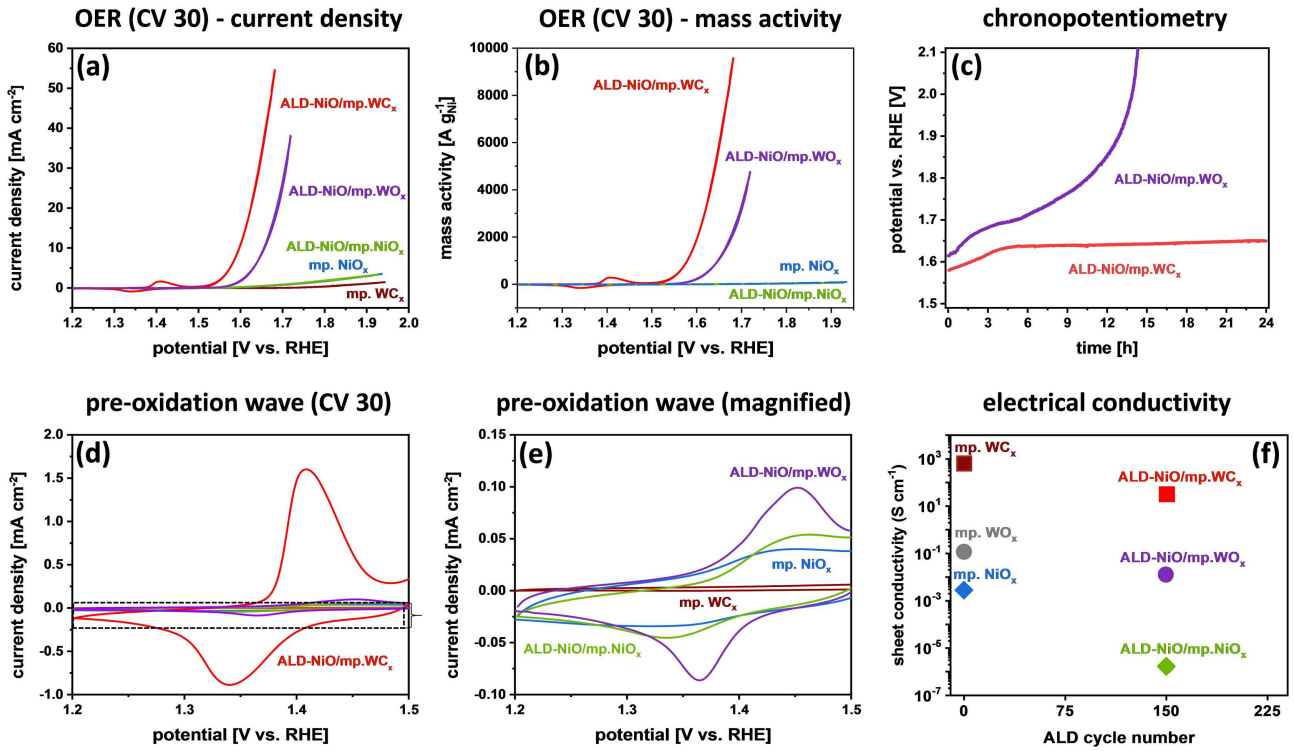

Figure 3. (a) CVs of ALD-NiO/mp. WC_x, bare mp. WC_x carrier, pristine mp. NiO_x, ALD-NiO/mp. WO_x, and ALD-NiO/mp. NiO_x using a RDE setup and N_2-purged 0.1 M KOH at 25 °C. The 30th CV is plotted for each catalyst system. (b) Mass activities of ALD-NiO/mp. WC_x, pristine mp. NiO_x, ALD-NiO/mp. WO_x, and ALD-NiO/mp. NiO_x derived from CVs plotted in (a), normalized by Ni contents. (c) Chronopotentiometric stability test of ALD-NiO/mp. WC_x and ALD-NiO/mp. WO_x for 24 h with a constant current density of 10 mA cm^{-2} in 0.1 KOH at 25 °C. (d) Pre-oxidation wave of $Ni^{2+/3+}$ enlarged from the 30th CVs in (a). (e) Enlarged section of (d) in a lower current density range from −0.075 to 0.012 mA cm^{-2}. Note that the red curve has been removed for the sake of clarity. (f) Electrical sheet conductivities assessed by impedance spectroscopy of bare mp. WC_x, mp. WO_x, mp. NiO_x carriers, and the ALD-NiO/mp. WC_x, ALD-NiO/mp. WO_x, and ALD-NiO/mp. NiO_x. All investigated films were deposited on flat, insulating glass substrates for the impedance spectroscopy measurements at $T = 25$ °C.

the Ni content (Figure 3b). The latter was determined by using inductively coupled plasma optical emission spectrometry (ICP-OES, Table 1). In addition, for the most active catalyst system, StrataGem/WDX analysis was performed to confirm the Ni loading without dissolution of the material. At a potential of 1.60 V vs. RHE, ALD-NiO/mp. WC_x reaches a Ni-mass based OER activity of 1989 A g^{-1}, which is ~9-fold higher than that of ALD-NiO/mp. WO_x, ~221-fold higher than that of pristine mp. NiO_x, and ~284-fold higher than that of ALD-NiO/mp. NiO_x. The outstanding Ni mass-specific activity of the ALD-NiO/mp. WC_x electrocatalyst can be explained by the ultra-low loading and high accessibility of the well-dispersed NiO active centers at the entire surface of the porous carrier film. Beyond that, a comparison of OER activities with state-of-the-art Ni-based catalysts highlights the superior OER activity of ALD-NiO/mp. WC_x (Table 2). In this context, it has to be noted that the herein developed catalyst does not suffer from any blocking of active sites by Nafion binder species.[59]

Moreover, the Tafel slopes (Figure S5) of the electrocatalysts were derived from the CV curves shown in Figure 3a. Pristine

Table 2. RDE-OER performance of highly efficient nickel-based electrocatalysts in alkaline electrolyte at RT reported in literature. Unless otherwise stated, the supporting electrolyte refers to unpurified KOH electrolyte which is expected to contain trace amounts of Fe impurities.

Catalyst	Electrolyte	Electrode type[a]	Binder	Tafel slope [mV dec^{-1}]	Overpotential[b] [V]	Mass activity[c] [A g^{-1}]	Reference
ALD-NiO/mp. WC_x	0.1 M KOH	Ti chip	binder-free	57	0.36	1989 (1.60 V_{RHE})	this work
mp. NiO_x	0.1 M KOH	Ti chip	binder-free	-	0.43 ($j = 1$ mA cm^{-2})	*n. a.*	[24]
NiO-ALD	1.0 M KOH (Fe-saturated)	FTO	binder-free	30	0.48	*n. a.*	[18]
LDH/G/Ni	0.1 M KOH	Ni-foam	binder-free	44	0.33	23 (1.60 V_{RHE})	[59]
NiO-$(La_{0.613}Ca_{0.387})_2NiO_{3.562}$	0.1 M KOH	GC	Nafion	42	0.37	52 (1.63 V_{RHE})	[61]
Ru_3Ni_1NAs	0.1 M KOH	GC	Nafion	152	0.38	*n. a.*	[62]
$NiFe_2O_4$	0.1 M KOH	GC	Nafion	80	0.37	11 (1.70 V_{RHE})	[63]
FeNC sheet/NiO	0.1 M KOH	carbon paper	Nafion	76	0.39	*n. a.*	[64]
ALD-NiO/CNT	1.0 M KOH (Fe-free)	GC	Nafion	50	0.32	*n. a.*	[27]
Ni/WC composite	0.1 M KOH	GC	Nafion	52	0.32	~530[d]	[60]

[a] GC = glassy carbon. [b] Overpotential at a current density of $j = 10$ mA cm^{-2}, unless otherwise stated. [c] Mass activities calculated based on the loading amounts of active species in the catalysts. [d] Mass activity estimated from compositional analysis by EDX (catalyst composition of $Ni_{1.77}WC$ assumed) and LSV curve in 1.0 M KOH.

mp. NiO_x and ALD-NiO/mp. NiO_x feature large Tafel slopes of 138 and 154 mV dec^{-1}, corresponding fairly well to the typical Tafel slope of pristine NiO reported in literature (see Table 2). In contrast, ALD-NiO/mp. WC_x exhibits a significantly reduced Tafel slope of 57 mV dec^{-1}, indicating remarkably faster reaction kinetics. Interestingly, the Tafel slope of ALD-NiO/mp. WC_x resembles that of ALD-NiO/CNT in our previous work,[27] further highlighting that applying a highly conductive substrate can significantly enhance the performance of a NiO-containing electrocatalyst.

Beside a high catalytic activity, a sufficient stability represents a key challenge of carbon-based support materials in OER catalysis under oxidative potentials. Hence, the stability of ALD-NiO/mp. WC_x was examined as a next step (Figure 3c). In the initial phase of the chronopotentiometric stability test, a slight increase in potential is visible, which originates from the oxidation of residual carbon species either from an incomplete decomposition of the polymer template or from the carburization step. In addition, a slight surface oxidation process at the carbide-NiO interface occurs, as described in the following. After reaching a stable state after about 4 h of testing, the catalytic activity of ALD-NiO/mp. WC_x remained stable until the end of the stability test over 24 h, providing strong evidence that the ALD-derived NiO coating is indeed effective in preventing an oxidative degradation of the bulk of the porous tungsten carbide scaffold. Contrarily, ALD-NiO/mp. WO_x did not reach a stable performance during the stability test, which is a consequence of an ongoing loss of active material by means of dissolution into the electrolyte. After about 14 h, most of the active material was dissolved into the surrounding electrolyte, resulting in a steep increase in potential. High-resolution TEM (HR-TEM) images of post-OER ALD-NiO/mp. WC_x scrapped off from the Ti substrate were taken (Figure S6-I). From the representative HR-TEM images, the crystallinity of both mp. WC_x carrier and NiO layer can still be claimed, which is further underlined by SAED analysis (see the Supporting Information, Section 6 for details). Ultimately, the existence of the thin NiO layer is proposed to effectively protect the WC_x carrier from pronounced bulk oxidation during OER, leading to the observed high catalytic stability.

XPS depth profiling of the spent catalyst ALD-NiO/mp. WC_x revealed a surface-oxidation of the WC_x carrier during OER, yet the underlying carbide phase appears to be sufficiently stable against further oxidation (see the Supporting Information, Section 7). Song et al.[60] reported similar observations for Ni/WC composite nanoparticles. The formation of a Ni^0-rich shell was demonstrated to effectively prevent the WC from oxidation during RDE-OER measurements in 1.0 M KOH.

In the present work, highly conformal NiO-ALD (cf. Figure S1) ensures the development of nanostructured catalyst coatings with well-defined mesoporosity that is essentially preserved after OER testing (see the Supporting Information, Section 7).

Electrical properties, estimation of ECSA and DFT calculations

In order to understand the superior OER activity of the ALD-NiO/mp. WC_x electrocatalytic system, the electrical properties of the bare and the NiO-coated carrier materials were investigated (Figure 3f). The sheet conductivities of both mp. WC_x and ALD-NiO/mp. WC_x are several orders of magnitude higher than that of the other materials, leading to significantly enhanced kinetics of the ALD-NiO/mp. WC_x electrocatalyst,[9] which is further proven by its smaller Tafel slope.[9,27,60] Regarding the superior catalytic activity, calculations of the ECSA from the double-layer capacitance (Supporting Information, Section 8) provide deeper insights, as the significantly enhanced ECSA of ALD-NiO/mp. WC_x reveals an excellent active site accessibility, which can be attributed to the mesoporosity introduced by the mp. WC_x carrier. This highlights the excellent suitability of ALD for the introduction of active species onto the porous system of an inactive, yet highly conductive, carrier. Enlarging the CV curves in a lower potential range of 1.20–1.60 V vs. RHE (Figure 3d, e),

the pre-oxidation wave of $Ni^{2+/3+}$ located at approximately 1.42 V vs. RHE becomes evident.[9] Due to the fact that Ni^{3+} has been shown to be the main responsible species for high OER activity, particularly, the pre-oxidation of Ni^{2+} to Ni^{3+} is a crucial process to optimize the electrocatalytic behavior.[9] When comparing with ALD-NiO/mp. WO_x, ALD-NiO/mp. NiO_x and mp. NiO_x, the pre-oxidation wave for ALD-NiO/mp. WC_x is, on the one hand, more pronounced and, on the other hand, shifted to lower potentials. However, it has to be noted that the presence of trace Fe impurities in the KOH electrolyte alters both intensity and position of the reversible $Ni^{2/3+}$ redox peaks (see the Supporting Information, Section 4).[9,23,65] However, our experimental data reveal a significantly increased number of well-accessible active Ni^{3+} sites for ALD-NiO/mp. WC_x that finally lead to the excellent OER activity due to the systematic investigations and similar measurement conditions for all herein studied catalyst systems. In order to highlight the high intrinsic activity of the surface Ni species in ALD-NiO/mp. WC_x, additional electrochemical measurements using an extensively purified Fe-free KOH electrolyte were conducted (Figure S4-II).

To gain deeper insights into the experimentally observed carbide-promoted $Ni^{2+} \rightarrow Ni^{3+}$ transitions, DFT calculations using the Vienna ab initio simulation package (VASP)[66–69] and projector-augmented wave (PAW) approach of Joubert and Kresse[70,71] (see Computational details and Section 9 in the Supporting Information) were performed based on simplified structural slab models of a NiO-coated W_2C (100) surface and a bare NiO (100) surface as a reference. Therefrom, the reaction energies with *OH intermediate species during the initial phases of the OER process were calculated for both NiO-coated W_2C and NiO. The obtained free energies clearly reveal a pronounced beneficial impact of the underlying carbide layers on the adsorption of *OH intermediates on the surface-exposed NiO layer. Our theoretical results provide clear evidence for a more favorable adsorption of *OH intermediate species for the NiO-coated W_2C lattice compared to the NiO reference (Figure S9). Thus, the theoretical findings corroborate the experimentally observed enhanced conversion of Ni^{2+} into Ni^{3+} active sites for ALD-NiO/mp. WC_x. Ultimately, the high number of surface-exposed and well-accessible NiOOH structural motifs in ALD-NiO/mp. WC_x boosts its OER activity in alkaline electrolyte.

Conclusion

In summary, a synthesis route affording macroscopically crack-free, homogeneous mp. WC_x films with interconnected porosity by pseudomorphic carburization of a mp. WO_x precursor film was developed for the first time. A highly efficient ALD-NiO/mp. WC_x OER electrocatalyst was obtained by using highly conformal NiO-ALD on the mp. WC_x carrier. Despite the ultra-low loading, the NiO/WC_x electrocatalyst shows a moderate overpotential of 360 mV in 0.1 M KOH and a remarkably high Ni mass-based OER activity of 1989 $A\,g^{-1}$ as a result of the easily accessible active sites. In this system, the mp. WC_x carrier plays a crucial role in leading to this outstanding activity. On the one hand, the mp. WC_x provides a highly conductive mesoporous scaffold that largely enhances the kinetics of the entire system. On the other hand, the synergetic effects between NiO and mp. WC_x significantly improve the conversion from Ni^{2+} into Ni^{3+}, hence, it provides additional highly active sites for the electrocatalytic OER. In this context, theoretical calculations provide further evidence for a more favorable adsorption energy of *OH intermediate species with respect to bare NiO. All in all, a novel and highly promising mp. WC_x carrier film was developed, offering new approaches for the production of highly active electrocatalysts with excellent electrical properties. The present study serves as a proof-of-concept for the development of highly efficient electrocatalysts with maximized utilization of active species provided by conformal ALD on porous metal carbide scaffolds. Future works will focus on controlled surface modifications of different mesoporous carbide carriers, for example with binary metal oxides such as Co–Ni oxides or noble metal species.

Experimental Section

Synthesis of mesoporous films

Different substrates were used for the deposition of the materials. Single-side polished silicon (Si) wafers obtained from University Wafers with (100) orientation were cleaned with EtOH after a thermal treatment in air for 2 h at 600 °C prior to film deposition. For the electrical sheet conductivity measurements by using impedance spectroscopy, insulating quartz glass (SiO_2) substrates (Science Services GmbH) were used and cleaned using a mixture of KOH and *i*PrOH prior to film deposition. Electrochemical measurements were performed using conductive titanium (Ti) substrates, polished with a 0.02 μm colloidal silica suspension (amorphous; Buehler, MasterMet 2) and cleaned using a 1 : 1 mixture of EtOH and *i*PrOH.

For the synthesis of mesoporous WO_x films, anhydrous tungsten(VI) chloride (WCl_6, > 99.9 % trace metals basis) was purchased from Merck. Citric acid (> 99.5 %, reagent grade) and ethanol (≥ 99.8 %) were purchased from VWR Chemicals. As structure-directing agent, a triblock copolymer PEO-PB-PEO, composed of 20400 $g\,mol^{-1}$ polyethylene oxide (PEO) and 10000 $g\,mol^{-1}$ polybutadiene (PB) was purchased from Polymer Service Merseburg GmbH.[8] All chemicals were used as received without any further purification. In a typical synthesis, the PEO-PB-PEO polymer template (55 mg) was dissolved in EtOH (1.50 mL) at 45 °C (Ar). A clear solution was obtained after stirring for 2 h at 45 °C (**I**). In another vial, WCl_6 (397 mg, 1.0 mmol) was dissolved in EtOH (1.50 mL; Ar) under stirring. Citric acid (384 mg, 2.0 mmol; 2.0 eq.) were added under stirring (Ar) affording a clear dark blue solution (**II**). The addition of citric acid led to a change from a dark green to a dark blue solution, indicating the formation of a metal-ligand complex, as described by Eckhardt et al.[44] for different metal ions in previous works. After stirring for 30 min at 45 °C (Ar), solution (**I**) was added. After stirring for a further 2 h at 45 °C (Ar), the obtained clear dark blue solution (**III**) was transferred into a Teflon cuvette (preheated to 45 °C) and dip-coating was performed in a controlled atmosphere in air (T = 25 °C, relative humidity of 35–40 %) on different substrates with a withdrawal rate of 300 $mm\,min^{-1}$. The films were dried for at least 5 min in the controlled atmosphere. After calcination in nitrogen atmosphere for 5 h at 500 °C with a heating ramp of 2 $K\,min^{-1}$, colored films were obtained.

The obtained mp. WO_x films were converted into mp. WC_x films with well-preserved nanocrystallinity and porous structure by carburization in a ternary gas mixture of CH_4, H_2 and Ar. The ratio of CH_4:H_2 during the carburization step for 6 h at 700 °C in a large tube furnace was set to 6:1. A heating rate of 1 K min^{-1} was used. The films were passivated after reaching RT in a mixture of 1% O_2/Ar for at least 3 h. For the removal of surface coke deposits on the materials, another heat treatment for 2 min at 550 °C in air was performed. Dark grey films were obtained.

For the synthesis of mp. NiO_x films, a previously established method by Bernicke et al.[24] was used. In brief, dip-coating solutions were prepared by dissolving a triblock-copolymer template (PEO_{213}-PB_{184}-PEO_{213}; 60 mg) in EtOH (3.0 mL). The solution was stirred for 2 h at 45 °C. Then, citric acid (144 mg) and $Ni(NO_3)_2 \cdot 6H_2O$ (436.0 mg; NeoLab, 98%) were added. The obtained clear green solution was transferred into a cuvette placed inside a dip-coater at 25 °C and a relative humidity of 40%. After drying, the samples were heated with 2 K min^{-1} to 250 °C and after 1 h at 250 °C, temperature was increased with a ramp of 2 K min^{-1} to 400 °C and again held for 1 h.

NiO-ALD

Nickelocene (Bis(cyclopentadienyl)nickel, $Ni(Cp)_2$, 99%) was purchased from STREM Chemicals Inc. Ozone (O_3) was generated using oxygen (99.99%) at a pressure of 0.5 bar in a BMT803N ozone generator. The estimated concentration of ozone delivered to the ALD system was 60–70 g Nm^{-3}. Argon, nitrogen, and oxygen were provided by Air Liquide (99.99% purity). NiO was directly deposited on the mesoporous WC_x, WO_x and NiO_x films on flat Ti, Si or quartz substrates. Moreover, pre-cleaned single-side polished Si wafers (Siegert Wafer B014002) with a native SiO_2 layer (about 1.2–1.8 nm) were also added into the ALD chamber for calibration of the NiO-thickness by spectroscopic ellipsometry (SE). ALD was performed in a commercial ALD system by ARRADIANCE (GEMStar-6). The comprehensive of the experimental procedure can be found elsewhere.[27,51,52] In brief, nickelocene (contained in a stainless-steel canister at 90 °C) and O_3 (as generated at RT) were used as metal precursor and oxygen source, respectively. The precursors were supplied using two separate manifolds for metal precursor and oxygen source that were maintained at 120 °C and 100 °C, respectively. Ar was used as a carrier and purging gas for the precursors to the reaction chamber, and to remove any of the excess reactants and by-products. Additionally, an Ar booster was used as pulsed-vapor-push method (PVP^{TM}) to carry out nickelocene vapors to the reaction chamber. The ALD system was evacuated (approx. $7.5 \cdot 10^{-3}$ mbar), and the temperature of the ALD reaction chamber was stabilized at 200 °C before starting the deposition. Prior to ALD, all samples were treated in situ with UV-O_3 (5 cycles of 0.5 s O_3 pulse/30 s exposure/15 s purge; total exposure time = 150 s) to remove any residual surface organic impurities and to functionalize the surface, thereby promoting the chemisorption of the nickelocene species. The ALD cycle was adjusted as a sequence of pulse/exposure/purge time as 1.2 s/20 s/30 s and 0.2 s/20 s/30 s for $Ni(Cp)_2$ and O_3, respectively.

Characterization

SEM images were recorded at 20 kV on a JEOL 7401F. The obtained SEM images were evaluated with ImageJ freeware, version 1.48 (www.imagej.nih.gov/ij). Corresponding FFT images were created using this software.

TEM images were taken using a FEI Tecnai G2 20 S-TWIN and a FEI Talos transmission electron microscopes at 200 kV acceleration voltage on scraped-off film fragments deposited on carbon-coated copper grids. A FEI Talos EDX detector was used to collect the elemental mapping for the samples. The EDX elemental mappings were analyzed using FEI Velox software version 2.6. The obtained TEM images and SAED patterns were evaluated with *ImageJ* freeware.

X-ray photoelectron spectra (XPS) were obtained using a Thermo Fisher Scientific ESCALAB 250Xi featuring a spot size of 400 μm, K-alpha X-rays. The peak position of adventitious carbon (284.80 eV) was used in order to correct the binding energy of the obtained spectra. The fitting of the XPS spectra and the quantification of the elemental composition was processed by the software Avantage. The XPS depth profile was measured with 3 cycles of Ar monatomic ion gun etching. The measurement was in low current, single phase etching mode, ion energy for the etching was 4000 eV. Raster size was 1 mm. The sputter rate using Ta_2O_5 as a reference amounts to 0.74 nm s^{-1}.

For the ICP-OES measurements, mesoporous films deposited on Si and on Ti substrates were used after dissolution in acid. Measurements were conducted on a Varian ICP-OES 715 ES (radial configuration). For calibration, aqueous solutions containing both Ni and W (Carl Roth) were prepared. For the calculation of the geometric Ni loading, the geometric areas of the films were evaluated using ImageJ software prior to dissolution of the materials. Each film was digested using a mixture of MilliQ H_2O (1.50 mL) and concentrated HNO_3 (1.50 mL; 65%, Carl Roth) under the application of ultrasound for 4 h at 60 °C. Complete dissolution was indicated by the bare polished wafer surface becoming visible for all investigated samples after the digestion step. Similar geometric Ni loadings were obtained for films deposited on Si and Ti substrates. Alternatively, the evaluation of the geometric loading of the synthesized films, wavelength-dispersive X-ray spectroscopy (WDX) was performed using StrataGem film analysis software (v. 4.8). Five independent measurements were conducted for the most important sample of the study-ALD-NiO/mp. WC_x-using a JEOL JXA-8530F electron microprobe at 10 kV. The mass depth of all components of the analyzed film amounts to an average of 96 ± 1 μg cm^{-2}. Cross-sectional SEM revealed an average sheet thickness of 230 nm (see the Supporting Information Figure S3-II).

The surface areas were measured by Kr-physisorption at 77 K on an Autosorb-iQ (Quantachrome) cooled with liquid N_2. Films were deposited on both sides of double-side polished Si wafers. Prior to the measurements, all samples were degassed for 2 h at 150 °C under vacuum. The geometric areas of the investigated films was analyzed using ImageJ freeware. Finally, the surface areas were calculated by using the well-established Brunauer-Emmett-Teller (BET) method. Note that for the analysis of the NiO-coated samples, the ALD process was applied twice to ensure coating of both sides on the substrate (successful loading was checked for both sides by EDX in a SEM at 20 kV acceleration voltage).

Values for the electrical sheet conductivities were calculated by impedance spectroscopy measurements in a home-built setup in the dark. The measurements were performed using a 8×8 gold pin array as probe head with an altering polarity sequence. A SP-200 potentiostat (Biologic) was used in a range between 100 mHz and 1 kHz. The obtained spectra (Nyquist impedance) were fitted using EIS Zfit software (EC-Lab v. 11.33, Biologic). All values are stated after normalization to the respective film thickness of the investigated material, which was obtained through cross-section SEM. All materials were deposited on insulating quartz glass substrates for the impedance measurements.

Pre-cleaned Si wafers (SSP, Siegert wafer B014002) with a native SiO_2 layer of approximately 1.2–1.8 nm were added into the ALD chamber to calibrate the NiO thickness by spectroscopic ellipsom-

etry (SE). The data were modelled using the software SpectraRay-3 (Si/SiO_2/NiO, Cauchy-stack and Lorentz–Lorenz model for SiO_2 and NiO, respectively).

Electrochemistry

Electrocatalytic testing was performed in a three electrode rotating disc setup (RDE) using a reversible hydrogen electrode (Gaskatel, HydroFlex) as a reference and a Pt gauze (Chempur, 1024 mesh cm^{-2}, a wire diameter of 0.06 mm, 99.9% purity) as counter electrode at 25 °C. All potentials are referred to reversible hydrogen electrode (RHE) and are *iR*-corrected to account for Ohmic losses in the setup. For the investigations of the OER activity, mesoporous films coated on a spherical Ti chip of 5 mm diameter were mounted on a rotating disc shaft serving as working electrode. A constant rotation of 1600 rpm was set. 0.1 M KOH was used as supporting electrolyte (Sigma Aldrich, pellets, 99.99% trace metals basis, purity excluding sodium content) and a SP-200 as potentiostat. The electrolyte solution was purged with N_2 for at least 30 min prior to catalytic testing. The OER activity was investigated by cyclic voltammetry (CV) between 1.20 and 1.95 V vs. RHE at a scan rate of 6 mV s^{-1}. It has to be noted that no electrochemical activation of the films has been performed, which is known to increase the observed OER activities for NiO electrocatalysts.[24]

For the evaluation of the double-layer capacitance (C_{dl}) and determination of the ECSA, after 50 CVs in OER regime, cycling with increasing scan rates of 50, 75, 100, 125, and 150 mV s^{-1} was performed in a lower potential range between 0.40 to 1.40 V vs. RHE at 25 °C. At each scan rate, five consecutive CVs were recorded. *iR*-corrections were applied for each scan rate. For the calculation of the double-layer capacitance from CV, the average values of the anodic and cathodic current densities at 0.90 V vs. RHE were used. By dividing C_{dl} by the specific capacitance of the sample (C_s = 0.040 mF cm^{-2} stated by McCrory et al.[72]), the ECSA can be calculated.

For the chronopotentiometric stability testing, mesoporous films coated on a conductive Ti substrate, to which a piece of Ti wire was attached by welding, were used. The relative geometric areas of the mesoporous films were measured using ImageJ software and the current densities were set to 10 mA cm^{-2} OER during chronopotentiometry in 0.1 M KOH at 25 °C.

Computational details

All calculations were carried out with the plane wave Vienna ab initio simulation package VASP,[66–69] version 6.1.1/6.1.2, using the projector-augmented wave (PAW) approach of Joubert and Kresse.[70,71] The PBE functional[73] was applied. London dispersion effects were taken into account by the D3 correction with Becke–Johnson damping.[74–77] The respective PAW parameters were extracted from the VASP POTCAR files library, C 08Apr2002 [4 valence electrons (VE)], W 08Apr2002 (6 VE), Ni 02Aug2007 (10 VE), O 08Apr2002 (6 VE), H 15Jun2001 (1 VE). The energy cutoff was set to 900 eV, except for the adsorbed *OH species on ALD-NiO/mp. WC_x with 600 eV and the gas phase molecules H_2O and H_2 with 450 eV. For the WC_x carrier material, a simplified description using the predominant W_2C phase was established. Preliminary tests for the W_2C bulk revealed that its ground state is non-magnetic. Thus, restricted Kohn–Sham calculations were performed for this system. In all calculations, for NiO an antiferromagnetic state was assumed by defining alternating magnetic moments on the Ni atoms, but without fixing the total magnetic moment during the SCF procedure. The space groups of NiO and W_2C are $Fm\bar{3}m$[78] and $P\bar{3}1m$,[79] respectively. For the antiferromagnetic ground state of NiO, a [(0,1,1),(1,0,1),(1,1,0)] supercell was built. The crystal structure of W_2C, which includes partial occupations of Wyckoff sites 2c and 2d by the carbon atoms, was simplified and all carbon atoms were placed on 2d (1/3, 2/3, 1/2) Wyckoff positions. For the surface optimization, the lattice constants were fixed at the optimized bulk values and only the atomic positions were relaxed. The Monkhorst–Pack k-point grids were set to 4×4×4 for the NiO and W_2C bulk and to 4×4×1 for the surface calculations. To receive the antiferromagnetic order in NiO in the (100) surface, a 2×1-supercell of a (121)-cut of the bulk supercell was set up. The surface models were composed of six stoichiometric layers for NiO and five W_2C layers with one NiO layer at both top and bottom for the NiO-covered W_2C models. The vacuum distance was set to 12 Å, convergence was tested for adsorption of oxygen species for similar systems. Convergence criteria were set to 10^{-6} eV for the chronopotentiometric electronic self-consistent cycle and 0.01 eV $Å^{-1}$ for structure optimization.

Acknowledgements

The authors thank ZELMI (TU Berlin) for access to TEM and SAED analyses and gratefully acknowledge financial support by BMBF (Bundesministerium für Bildung und Forschung) ATO-KAT: Atomar dünn beschichtete poröse Elektroden als neuartige Katalysatoren für die Wasser-Elektrolyse (03EK3052A, 03EK3052C). A.A. and R.K. gratefully acknowledge funding through the DFG SPP 2080 priority program (KR 3920/4-1). Arne Thomas (TU Berlin) is thankfully acknowledged for providing access to XPS analyses. Christoph Erdmann (HU Berlin) is acknowledged for HRTEM, SAED, HAADF-STEM, and elemental mapping measurements. The authors thank Jörg Nissen (TU Berlin, ZELMI) very much for WDX/StrataGem analyses and Astrid Kluge (TU Berlin) for performing ICP-OES measurements and calibration. Benjamin Paul (TU Berlin) is thankfully acknowledged for assistance in building a setup for impedance spectroscopy measurements of thin films in the dark. Open Access funding enabled and organized by Projekt DEAL.

Conflict of Interest

The authors declare no conflict of interest.

Keywords: atomic layer deposition · electrocatalysis · metal carbides · mesoporous materials · nickel

[1] Y. Xu, M. Kraft, R. Xu, *Chem. Soc. Rev.* **2016**, *45*, 3039–3052.
[2] J. Li, Y. Wang, T. Zhou, H. Zhang, X. Sun, J. Tang, L. Zhang, A. M. Al-Enizi, Z. Yang, G. Zheng, *J. Am. Chem. Soc.* **2015**, *137*, 14305–14312.
[3] J. Wang, W. Cui, Q. Liu, Z. Xing, A. M. Asiri, X. Sun, *Adv. Mater.* **2016**, *28*, 215–230.
[4] S. Cobo, J. Heidkamp, P.-A. Jacques, J. Fize, V. Fourmond, L. Guetaz, B. Jousselme, V. Ivanova, H. Dau, S. Palacin, M. Fontecave, V. Artero, *Nat. Mater.* **2012**, *11*, 802–807.
[5] J. Kim, X. Yin, K.-C. Tsao, S. Fang, H. Yang, *J. Am. Chem. Soc.* **2014**, *136*, 14646–14649.
[6] N.-T. Suen, S.-F. Hung, Q. Quan, N. Zhang, Y.-J. Xu, H. M. Chen, *Chem. Soc. Rev.* **2017**, *46*, 337–365.
[7] M. Ye, S. Li, X. Zhao, N. V. Tarakina, C. Teutloff, W. Y. Chow, R. Bittl, A. Thomas, *Adv. Mater.* **2020**, *32*, 1903942.

[8] E. Ortel, T. Reier, P. Strasser, R. Kraehnert, *Chem. Mater.* **2011**, *23*, 3201–3209.
[9] M. Görlin, J. Ferreira de Araújo, H. Schmies, D. Bernsmeier, S. Dresp, M. Gliech, Z. Jusys, P. Chernev, R. Kraehnert, H. Dau, P. Strasser, *J. Am. Chem. Soc.* **2017**, *139*, 2070–2082.
[10] M. Biegun, X. Chen, E. Mijowska, *ChemElectroChem* **2018**, *5*, 2681–2685.
[11] T. Reier, M. Oezaslan, P. Strasser, *ACS Catal.* **2012**, *2*, 1765–1772.
[12] D. V. Esposito, J. G. Chen, *Energy Environ. Sci.* **2011**, *4*, 3900.
[13] Y.-J. Wang, D. P. Wilkinson, J. Zhang, *Chem. Rev.* **2011**, *111*, 7625–7651.
[14] A. S. Aricò, P. Bruce, B. Scrosati, J.-M. Tarascon, W. van Schalkwijk, *Nat. Mater.* **2005**, *4*, 366–377.
[15] X. Li, X. Hao, A. Abudula, G. Guan, *J. Mater. Chem. A* **2016**, *4*, 11973–12000.
[16] J. W. D. Ng, M. García-Melchor, M. Bajdich, P. Chakthranont, C. Kirk, A. Vojvodic, T. F. Jaramillo, *Nat. Energy* **2016**, *1*, 16053.
[17] T. Zhang, M.-Y. Wu, D.-Y. Yan, J. Mao, H. Liu, W.-B. Hu, X.-W. Du, T. Ling, S.-Z. Qiao, *Nano Energy* **2018**, *43*, 103–109.
[18] K. L. Nardi, N. Yang, C. F. Dickens, A. L. Strickler, S. F. Bent, *Adv. Energy Mater.* **2015**, *5*, 1500412.
[19] M. Gong, Y. Li, H. Wang, Y. Liang, J. Z. Wu, J. Zhou, J. Wang, T. Regier, F. Wei, H. Dai, *J. Am. Chem. Soc.* **2013**, *135*, 8452–8455.
[20] D. Bernsmeier, M. Bernicke, R. Schmack, R. Sachse, B. Paul, A. Bergmann, P. Strasser, E. Ortel, R. Kraehnert, *ChemSusChem* **2018**, *11*, 2367–2374.
[21] F. Lyu, Q. Wang, S. M. Choi, Y. Yin, *Small* **2019**, *15*, 1804201.
[22] M. Shao, Q. Chang, J.-P. Dodelet, R. Chenitz, *Chem. Rev.* **2016**, *116*, 3594–3657.
[23] M. Yu, G. Moon, E. Bill, H. Tüysüz, *ACS Appl. Mater. Interfaces* **2019**, *2*, 1199–1209.
[24] M. Bernicke, B. Eckhardt, A. Lippitz, E. Ortel, D. Bernsmeier, R. Schmack, R. Kraehnert, *ChemistrySelect* **2016**, *1*, 482–489.
[25] S. M. Bhaway, P. Tangvijitsakul, J. Lee, M. D. Soucek, B. D. Vogt, *J. Mater. Chem. A* **2015**, *3*, 21060–21069.
[26] D. Chandra, T. Sato, Y. Tanahashi, R. Takeuchi, M. Yagi, *Energy* **2019**, *173*, 278–289.
[27] Y. Fan, Y. Wu, G. Clavel, M. H. Raza, P. Amsalem, N. Koch, N. Pinna, *ACS Appl. Mater. Interfaces* **2018**, *1*, 4554–4563.
[28] S. Lu, J. Wu, H. Hu, X. Pan, Z. Hu, H. Li, H. Zhu, F. Duan, M. Du, *J. Colloid Interface Sci.* **2021**, *585*, 258–266.
[29] Y. Wang, S. Song, P. K. Shen, C. Guo, C. M. Li, *J. Mater. Chem.* **2009**, *19*, 6149.
[30] R. Sachse, D. Bernsmeier, R. Schmack, I. Häusler, A. Hertwig, K. Kraffert, J. Nissen, R. Kraehnert, *Catal. Sci. Technol.* **2020**, *10*, 2057–2068.
[31] D. Bernsmeier, R. Sachse, M. Bernicke, R. Schmack, F. Kettemann, J. Polte, R. Kraehnert, *J. Catal.* **2019**, *369*, 181–189.
[32] H. Jiang, J. Gu, X. Zheng, M. Liu, X. Qiu, L. Wang, W. Li, Z. Chen, X. Ji, J. Li, *Energy Environ. Sci.* **2019**, *12*, 322–333.
[33] J. Zhang, Z. Zhao, Z. Xia, L. Dai, *Nat. Nanotechnol.* **2015**, *10*, 444–452.
[34] J.-M. Giraudon, P. Devassine, J.-F. Lamonier, L. Delannoy, L. Leclercq, G. Leclercq, *J. Solid State Chem.* **2000**, *154*, 412–426.
[35] Z. Wu, Y. Yang, D. Gu, Q. Li, D. Feng, Z. Chen, B. Tu, P. A. Webley, D. Zhao, *Small* **2009**, *5*, 2738–2749.
[36] Y. Wang, C. He, A. Brouzgou, Y. Liang, R. Fu, D. Wu, P. Tsiakaras, S. Song, *J. Power Sources* **2012**, *200*, 8–13.
[37] A. Löfberg, A. Frennet, G. Leclercq, L. Leclercq, J. M. Giraudon, *J. Catal.* **2000**, *189*, 170–183.
[38] Q. Gong, Y. Wang, Q. Hu, J. Zhou, R. Feng, P. N. Duchesne, P. Zhang, F. Chen, N. Han, Y. Li, C. Jin, Y. Li, S.-T. Lee, *Nat. Commun.* **2016**, *7*, 13216.
[39] Z. Chen, W. Gong, S. Cong, Z. Wang, G. Song, T. Pan, X. Tang, J. Chen, W. Lu, Z. Zhao, *Nano Energy* **2020**, *68*, 104335.
[40] D. Chatzikyriakou, N. Krins, B. Gilbert, P. Colson, J. Dewalque, J. Denayer, R. Cloots, C. Henrist, *Electrochim. Acta* **2014**, *137*, 75–82.
[41] G. A. Niklasson, L. Berggren, A.-L. Larsson, *Sol. Energy Mater. Sol. Cells* **2004**, *84*, 315–328.
[42] O. Ostrovski, G. Zhang, *AIChE J.* **2006**, *52*, 300–310.
[43] H. Wang, G. Li, J. Ma, D. Zhao, *RSC Adv.* **2017**, *7*, 3921–3927.
[44] B. Eckhardt, E. Ortel, J. Polte, D. Bernsmeier, O. Görke, P. Strasser, R. Kraehnert, *Adv. Mater.* **2012**, *24*, 3115–3119.
[45] T. Brezesinski, D. Fattakhova Rohlfing, S. Sallard, M. Antonietti, B. M. Smarsly, *Small* **2006**, *2*, 1203–1211.
[46] S. Sallard, T. Brezesinski, B. M. Smarsly, *J. Phys. Chem. C* **2007**, *111*, 7200–7206.
[47] T. Brezesinski, M. Groenewolt, A. Gibaud, N. Pinna, M. Antonietti, B. Smarsly, *Adv. Mater.* **2006**, *18*, 2260–2263.
[48] C. J. Brinker, Y. Lu, A. Sellinger, H. Fan, *Adv. Mater.* **1999**, *11*, 579–585.
[49] D. Grosso, F. Cagnol, G. J. de A. A. Soler-Illia, E. L. Crepaldi, H. Amenitsch, A. Brunet-Bruneau, A. Bourgeois, C. Sanchez, *Adv. Funct. Mater.* **2004**, *14*, 309–322.
[50] T. Fontecave, C. Boissiere, N. Baccile, F. J. Plou, C. Sanchez, *Chem. Mater.* **2013**, *25*, 4671–4678.
[51] M. H. Raza, N. Kaur, E. Comini, N. Pinna, *ACS Appl. Mater. Interfaces* **2020**, *12*, 4594–4606.
[52] M. H. Raza, K. Movlaee, S. G. Leonardi, N. Barsan, G. Neri, N. Pinna, *Adv. Funct. Mater.* **2020**, *30*, 1906874.
[53] X. Tong, Y. Qin, X. Guo, O. Moutanabbir, X. Ao, E. Pippel, L. Zhang, M. Knez, *Small* **2012**, *8*, 3390–3395.
[54] M. C. Biesinger, B. P. Payne, A. P. Grosvenor, L. W. M. Lau, A. R. Gerson, R. S. C. Smart, *Appl. Surf. Sci.* **2011**, *257*, 2717–2730.
[55] H. Wu, J. Geng, H. Ge, Z. Guo, Y. Wang, G. Zheng, *Adv. Energy Mater.* **2016**, *6*, 1600794.
[56] J. Liu, Y. Nan, X. Chang, X. Li, Y. Fang, Y. Liu, Y. Tang, X. Wang, R. Li, J. Ma, *Int. J. Hydrogen Energy* **2017**, *42*, 10802–10812.
[57] X. Wu, X. Han, X. Ma, W. Zhang, Y. Deng, C. Zhong, W. Hu, *ACS Appl. Mater. Interfaces* **2017**, *9*, 12574–12583.
[58] C. Tang, H.-F. Wang, X. Chen, B.-Q. Li, T.-Z. Hou, B. Zhang, Q. Zhang, M.-M. Titirici, F. Wei, *Adv. Mater.* **2016**, *28*, 6845–6851.
[59] H.-F. Wang, C. Tang, Q. Zhang, *J. Mater. Chem. A* **2015**, *3*, 16183–16189.
[60] D. Song, J. Shin, Y. Lee, Y. Kwon, J. Lim, E.-J. Kim, S. Oh, M. Kim, E. Cho, *ACS Appl. Mater. Interfaces* **2019**, *2*, 3452–3460.
[61] R. Liu, F. Liang, W. Zhou, Y. Yang, Z. Zhu, *Nano Energy* **2015**, *12*, 115–122.
[62] J. Yang, Q. Shao, B. Huang, M. Sun, X. Huang, *iScience* **2019**, *11*, 492–504.
[63] C. Mahala, M. D. Sharma, M. Basu, *Electrochim. Acta* **2018**, *273*, 462–473.
[64] J. Wang, K. Li, H. Zhong, D. Xu, Z. Wang, Z. Jiang, Z. Wu, X. Zhang, *Angew. Chem. Int. Ed.* **2015**, *54*, 10530–10534; *Angew. Chem.* **2015**, *127*, 10676–10680.
[65] M. W. Louie, A. T. Bell, *J. Am. Chem. Soc.* **2013**, *135*, 12329–12337.
[66] G. Kresse, J. Hafner, *Phys. Rev. B* **1993**, *47*, 558–561.
[67] G. Kresse, J. Hafner, *Phys. Rev. B* **1994**, *49*, 14251–14269.
[68] G. Kresse, J. Furthmüller, *Comput. Mater. Sci.* **1996**, *6*, 15–50.
[69] G. Kresse, J. Furthmüller, *Phys. Rev. B* **1996**, *54*, 11169–11186.
[70] G. Kresse, D. Joubert, *Phys. Rev. B* **1999**, *59*, 1758–1775.
[71] P. E. Blöchl, *Phys. Rev. B* **1994**, *50*, 17953–17979.
[72] C. C. L. McCrory, S. Jung, J. C. Peters, T. F. Jaramillo, *J. Am. Chem. Soc.* **2013**, *135*, 16977–16987.
[73] J. P. Perdew, K. Burke, M. Ernzerhof, *Phys. Rev. Lett.* **1996**, *77*, 3865–3868.
[74] S. Grimme, J. Antony, S. Ehrlich, H. Krieg, *J. Chem. Phys.* **2010**, *132*, 154104.
[75] S. Grimme, S. Ehrlich, L. Goerigk, *J. Comput. Chem.* **2011**, *32*, 1456–1465.
[76] E. R. Johnson, A. D. Becke, *J. Chem. Phys.* **2005**, *123*, 024101.
[77] E. R. Johnson, A. D. Becke, *J. Chem. Phys.* **2006**, *124*, 174104.
[78] J. Zio'łkowski, L. Dziembaj, *J. Solid State Chem.* **1985**, *57*, 291–299.
[79] T. Epicier, J. Dubois, C. Esnouf, G. Fantozzi, P. Convert, *Acta Metall.* **1988**, *36*, 1903–1921.

Manuscript received: June 18, 2021
Revised manuscript received: August 11, 2021
Version of record online: September 8, 2021